

## A Pathfinder Instrument for Precision Radial Velocities in the Near-Infrared

L. W. RAMSEY,<sup>1</sup> J. BARNES,<sup>2</sup> S. L. REDMAN,<sup>1</sup> H. R. A. JONES,<sup>2</sup> A. WOLSZCZAN,<sup>1</sup>  
S. BONGIORNO,<sup>1</sup> L. ENGEL,<sup>1</sup> AND J. JENKINS<sup>1</sup>

*Received 2008 February 20; accepted 2008 June 20; published 2008 August 8*

**ABSTRACT.** We have designed and tested an in-plane echelle spectrograph configured to investigate precision radial velocities from ground-based near-infrared observations. The spectrograph operates across the spectral range of 0.9–1.7  $\mu\text{m}$  at a spectral resolution of  $R = 50,000$ , and uses a liquid nitrogen-cooled HAWAII 1 K detector. Repeated measurements of the Earth’s rotation via integrated sunlight with two different instrument arrangements in the near-infrared Y band have produced radial velocities with  $\sim 10 \text{ m s}^{-1}$  rms over a period of several hours. The most recent instrument configuration has achieved an unbinned rms of  $7 \text{ m s}^{-1}$  and suggests that infrared radial velocity precisions may be able to approach those achieved at optical wavelengths.

*Online material:* color figure

### 1. INTRODUCTION

The achievement of meter-per-second radial velocity precision is one of the major technological breakthroughs of recent years. Although this effort is frequently viewed as driven by the search for extrasolar planets following the discovery of the first such system in the early 1990s (Wolszczan & Frail 1992), the quest for highly accurate radial velocity measurements was actually under development for many decades beforehand. The path from solar studies (Becker 1976; Koch & Woehl 1984) to pioneering stellar observations using hydrogen fluoride (HF) gas cells (Campbell & Walker 1979; Campbell et al. 1988) to today’s standards of long-term several  $\text{m s}^{-1}$  (or short-term sub- $\text{m s}^{-1}$ ) rms measurements with Keck/HIRES (e.g., Vogt et al. 1994; Butler et al. 1996), ESO 3.6 m/HARPS (e.g., Pepe et al. 2000), HET/HRS (e.g., Tull 1998), VLT-UVES (Dekker et al. 2000), and AAT/UCLES (Tinney et al. 2001) is one that leads through several spectrographs, detectors, and calibration methodologies.

To date, the only astronomical programs that have yielded sub- $16 \text{ m s}^{-1}$  radial velocities are based on optical (500- to 600-nm) echelle spectroscopy, with velocity calibration based on  $\text{I}_2$  absorption or Th-Ar emission line references. While this wavelength region is optimal for investigating solarlike stars, it suffers when investigating cooler objects (especially in comparison with the infrared region). Main sequence M stars are particularly inviting targets for precision radial velocity work, both because these objects represent the most numerous class

of stars and because their low mass makes them promising objects for detection of Earth-mass planets in the “habitable zone” (Kasting & Catling, 2003). This is one of the top priorities of the Exoplanet Task Force.<sup>3</sup>

No instruments have published radial velocity results in the near-infrared with precisions approaching those in the optical, although exciting science results have been obtained in this wavelength region with hundreds of  $\text{m s}^{-1}$  precisions. For example, Stassun et al. (2006) characterized the orbital parameters of the brown dwarf binary 2MASS J05352184–0546085 using the PHOENIX spectrograph (Hinkle et al. 2003) on the Gemini South telescope. Using six nights of observations with NIRSPEC (McLean et al. 1998) at the Keck telescope, Martin et al. (2006) surpassed the precision achieved by previous optical radial velocity work on late-type stars; these infrared radial velocity measurements of the nearby brown dwarf LP944-20 report an rms precision of  $360 \text{ m s}^{-1}$ . Blake et al. (2007) used CO bands and telluric features to reach precisions of approximately  $300 \text{ m s}^{-1}$  around L dwarfs.

Moving beyond the CCD range to a wavelength regime where there is no tradition of precision ( $< 20 \text{ m s}^{-1}$ ) radial velocity studies are challenging because there is no legacy work to build upon. In time it should be possible to increase the sensitivity of tellurically calibrated programs down to mean atmospheric velocities of  $10\text{--}25 \text{ m s}^{-1}$  that have now been achieved in the optical (e.g., Johnston 2006; Gray & Brown 2006). However, more precise calibration techniques are

<sup>1</sup> Department of Astronomy and Astrophysics, The Pennsylvania State University, University Park, PA

<sup>2</sup> Centre for Astrophysics Research, University of Hertfordshire, College Lane, Hatfield AL10 9AB, UK

<sup>3</sup> More information on the Exoplanet Task Force is available online from the National Science Foundation, at [http://www.nsf.gov/mps/ast/aaac/exoplanet\\_task\\_force/reports/exoptf\\_final\\_report.pdf](http://www.nsf.gov/mps/ast/aaac/exoplanet_task_force/reports/exoptf_final_report.pdf).

required if infrared observations are to reach the  $\text{m s}^{-1}$  accuracy of current state-of-the-art optical projects.

This paper describes our experiments with a laboratory-based, high-resolution infrared spectrograph configured to measure precision radial velocities. This instrument, designated the Precision Radial Velocity Spectrograph Pathfinder (hereafter Pathfinder), was designed and constructed in the Department of Astronomy and Astrophysics at Penn State. The goal of this project was to measure the rotation velocity of the Earth by obtaining infrared spectra of integrated sunlight to explore the limitations of making precision radial velocities in the  $0.9\text{--}1.7\ \mu\text{m}$  spectral region. The most serious concern is the lack of a proven calibration technique. NIR arrays also have issues not present in CCDs, such as interpixel capacitance, multiplexer cross talk, persistence, and sensitivity to thermal background radiation. Telluric contamination is also a major issue in the NIR, as is modal noise, because the number of modes in optical fibers decreases with wavelength.

We carried out initial observations in 2006 August and, after a series of upgrades and intermediate tests, conducted another set of observations in 2007 November. Section 2 presents the design of the instrument and the properties of its various components. The data processing and analysis are described in § 3. Our conclusions, which point to the challenges that lie ahead, are given in § 4.

## 2. SPECTROGRAPH

The science requirement of measuring radial velocities to  $\text{m s}^{-1}$  accuracy in the infrared, with a very limited budget, required that the Pathfinder spectrograph cover the near-infrared regime (no K-band sensitivity) at a spectral resolution of several tens of thousand. Pathfinder is a brass board instrument that covers the Y, J, and H bands ( $0.9$  to  $1.7\ \mu\text{m}$ ) at a resolution of 50,000. The instrument was assembled using existing in-house optical components that were retired or borrowed from other projects.

The spectrograph is constructed primarily with standard optical mounting hardware on an  $8 \times 2$  foot optical bench, but the fiber input and the detector are mounted on custom-made units. This table is located in an interior lab that has controlled access. We did not have precision temperature monitoring hardware in place when the measurements discussed here were taken. However, recently installed Lakeshore PT102 platinum resistance thermometers with a Lakeshore 218 monitor indicate ambient room temperature variations are typically  $0.1\ \text{K}$  over several hours, while spectrograph temperature variations are on the order of  $0.05\ \text{K}$ . The spectrograph, located in an interior room in Davey Laboratory on the Penn State campus, is fed by a single fiber optic cable whose input end is located on the roof of the building in one of the rooftop observatories.

## 2.1. Optical Design

We will adopt the notation of Schroeder (2000) in our description of the Pathfinder optical design. An optical layout of the system is displayed in Figure 1. The instrument has a straightforward in-plane configuration with a R2 echelle and a 100-mm collimated beam diameter. The echelle is operated at an unusually large  $\theta$  angle of  $11.66^\circ$ , which is required to achieve the desired resolving power. The collimator is a simple 609-mm focal length parabola. The collimated beam is dispersed by a gold-coated 31-line  $\text{mm}^{-1}$   $\Theta_{\text{blaze}} = 63.4^\circ$  R2 echelle on a  $110 \times 210\ \text{mm}$  Zerodur substrate. Given that  $\theta = 11.66^\circ$ , the incident angle,  $\alpha = \Theta_{\text{blaze}} + \theta \approx 75^\circ$ , produces a substantial vignetting of the collimated beam by the  $200 \times 100\ \text{mm}$  ruled area of the grating. The effective collimated beam at the grating is 100 mm high and approximately 50 mm wide. The diffracted beam has an anamorphic magnification in the dispersion direction of  $\sim 2.3$  that is cross-dispersed by a 150-line  $\text{mm}^{-1}$   $\Theta_{\text{blaze}} = 2.15^\circ$  grating. The efficiency of this in-house (but far from optimal) cross-disperser is low ( $\sim 20\%$ ) in the wavelength band ( $0.95\text{--}1.35\ \mu\text{m}$ ) of our initial observations.

The Pathfinder camera is, like the collimator, a simple 154-mm diameter, 916-mm focal length parabola. A weak lens near the focus corrects much of the coma; this lens gives the camera an effective focal length of 800 mm. The camera beam is folded so as to allow the dewar to be mounted vertically. This configuration allows the detector coolant (liquid nitrogen; hereafter  $\text{LN}_2$ ) to always cover the cold plate on which the detector is mounted.

Figure 1 also shows the camera layout and spot diagram over the field of view of the detector in the focal plane. It is clear that the effects of coma are controlled to about 1 pixel at the edges of the detector; this is of considerable importance as there are only about 2.5 detector pixels per resolution element. The variation of the spot shape over the camera field imposes a limit on the

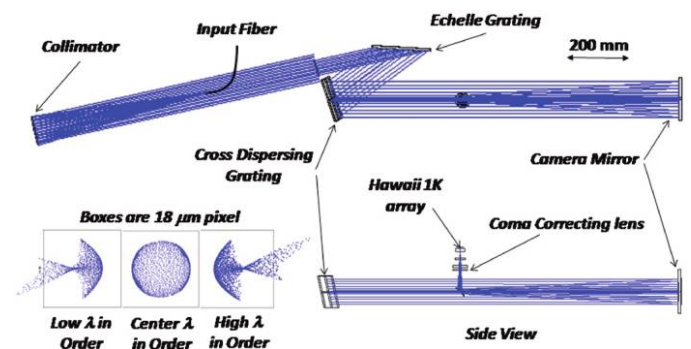


FIG. 1.—Optical layout from a Zemax model of the Pathfinder is illustrated as well as the theoretical imaging performance. The top of this figure is a top view in the plane of the echelle dispersion. The bottom right shows a side view from the cross-disperser to the final focal plane. The bottom left shows the expected spots at the center and edges of an order centered on the HAWAII 1 K array. The boxes are  $18\ \mu\text{m}^2$  and are approximately the size of one pixel.

radial velocity precision achievable in our system due to the limited number of calibration lines. As this is essentially a variation with wavelength, fundamentally the quantity we are measuring, it can only be well compensated if there is a calibration line in close proximity. While limited, this implementation was judged sufficient for our initial tests.

## 2.2. Detector and Dewar System

Pathfinder's detector is a HAWAII 1 K (1024 102<sup>2</sup>) science-grade array provided through IR Labs in Tucson Arizona and uses a SDSU Gen II controller. The dewar is cooled with LN<sub>2</sub>. Inside the dewar radiation shield, a filter holder is mounted to the same cooling block as the detector. The temperature is continuously monitored and is typically 82.3 K. The thermal background is suppressed with a 6-mm PK50 plate that attenuates radiation beyond 2  $\mu\text{m}$  and a short-pass filter with a cutoff at 1.8  $\mu\text{m}$  that has transmission less than  $10^{-3}$  out to 3  $\mu\text{m}$ . In operation the detector has a gain of 6.1  $e^-/\text{ADU}$  and a read noise of 20  $e^-$ . The bias voltage has been optimized for well capacity. We use single destructive readouts. Tests have shown that the linearity of the array is within 1% of linear for ADU counts below  $3 \times 10^4$ , which is our operational range. The effect of pixel-to-pixel variation of quantum efficiency, which is about 6.7% in our array, is reduced by averaging over the height of the spectrograph slit and by dividing by the flat-field spectra. As in any precision measurement, high S/N flat fields are crucial. The optical design yields a spectroscopic resolution of 50,000 with 2.5 pixels per resolution element ( $\sim 2.5 \text{ km s}^{-1} \text{ pixel}^{-1}$ ). At 1.0  $\mu\text{m}$  approximately 44% of the free spectral range (FSR) in an echelle order is covered by the detector; this value decreases to 33% at 1.6  $\mu\text{m}$ . Figure 2 illustrates the coverage of the detector in the 0.98–1.4  $\mu\text{m}$  region.

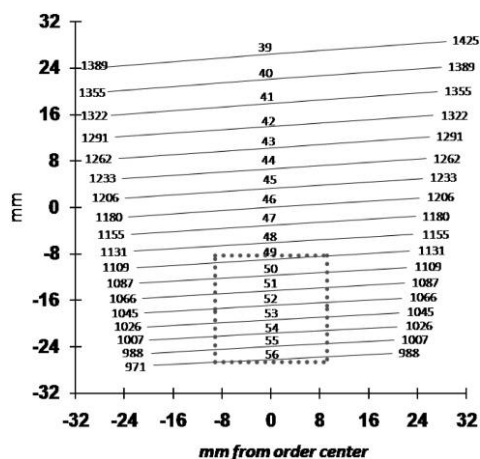


FIG. 2.—Each line represents one free spectral range of the order number given at the center. Beginning and ending wavelength in  $\mu\text{m}$  are also labeled. The coverage given by the array used by Pathfinder for the observations discussed here is shown by the dotted box. See the online edition of the PASP for a color version of this figure.

## 2.3. Fiber Input

For the 2006 August data set, a fiber slicer was used for the object input. Our slicer uses 100- $\mu\text{m}$  core, 125- $\mu\text{m}$  cladding diameter fibers; this yields a geometrical throughput of 49% after the Acrylate buffers are removed from the constituent fibers. The left panel of Figure 3 displays the input of the seven slicer fibers, and the middle panel is the output of the slicer fibers formatted into a pseudo-slit. The two outermost fibers on each end of the slit are the calibration lamp feeds. A single fiber spacer is used to separate each calibration fiber from the seven object fibers. Initial measurements of the laser output indicated acceptable focal ratio degradation. In 2007 October, we implemented a configuration with 300- $\mu\text{m}$  core fibers. The object fiber is separated from the calibration fiber by a single fiber spacer (see right panel in Fig. 3). To achieve our desired resolution the output end of the new input fiber cable was butted up against a 100- $\mu\text{m}$  slit on a 6-mm diameter stainless steel plate. In both instrument setups, we vibrated the fibers to minimize the effects of modal noise (Baudrand & Walker, 2001). By experiment, we found that this reduced the modal noise below the level of concern for this work. We have conducted extensive experiments on eliminating modal noise in the NIR, which will be detailed in a subsequent paper.

## 2.4. Control System

The echelle and cross-disperser gratings are mounted on rotational stages, and the camera is mounted on a linear stage. All three stages are driven with a DC servo motor with incremental encoder position feedback. A Newport ESP 300 motion controller with a RS232 interface to a PC are used for setting and tracking positions. Although we would prefer not to change the positions of the optics, the small size of the detector compared to the area covered by the spectral range of interest requires precision control of both the echelle and cross-disperser. The ability to establish and adjust focus with a precision control system is also highly desirable, although in practice the focus rarely needs adjustment.

## 2.5. Calibrations

The calibration unit contains Th-Ar, Ar, Kr, Ne, and Xe pen lamps as well as a quartz iodine flat-field lamp. Optical fibers are employed to combine the Nobel-gas lamp signals into a single integrating fiber. Th-Ar is the calibration of choice for most high-resolution spectrographs, but combining the Ar, Kr, Ne, and Xe lamps increased the number of available reference lines in the longer end of Pathfinder's waveband compared to the Th-Ar calibration. For the Y-band wavelength range presented here, we used the Ar pen lamp (2006) and Th-Ar lamp (2007).



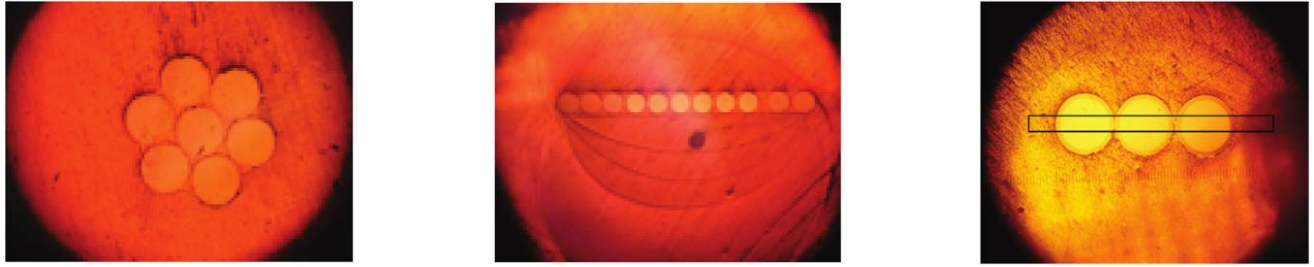


FIG. 3.—Photographs of the 2006 fiber slicer object input (*left*), fiber slicer pseudo slit with calibration fibers on each end (*middle*) for 2006 August data, and the fiber arrangement for 2007 November data with object, blank, and calibration fiber (*right*). The box in the 2007 November fiber arrangement shows the approximate location of a 100- $\mu\text{m}$  slit.

## 2.6. Solar Feed

The signal required for our experiment is the integrated solar disk; this is obtained by imaging the Sun onto a 50-m-long Polymicro FIP, 300- $\mu\text{m}$  core fiber that scrambles spatial information. The input end of the cable has a 2.5-mm ball lens with a  $10^\circ$  field of view, so tracking errors should not compromise obtaining integrated solar disk light. Unfortunately, we found that the field of view was so large that light scattered by nearby clouds noticeably degraded the quality of our signal, and so observations were only attempted when skies were mostly clear. Clouds that do not uniformly cover the Sun during an integration can lead to a significant solar rotation residual in the data as solar rotation is about 100 times greater than what we are trying to measure.

## 3. DATA REDUCTION AND ANALYSIS

To explore the issues involved in precision radial velocities in the NIR, we used the Earth's rotation signal, found in integrated sunlight. This signal has an amplitude of several hundred  $\text{m s}^{-1}$  and can be measured on any clear day in the laboratory avoiding the added time and expense of going to a remote telescope. Our program concentrated on a region of the Y band selected to have (1) relatively few strong telluric features, (2) numerous solar features, and (3) enough calibration lines to track spectrograph instabilities. The spectral region used is illustrated in Figure 4 and provided wavelength coverage between 1.03 and 1.103  $\mu\text{m}$ .

While we have experimented with numerous instrument configurations, we will only discuss initial and most recent tests. On 2006 August 16, we acquired 781 10-s exposures using the fiber setup shown in the left and middle images of Figure 3 (hereafter the 2006 data set). This slicer produced spectra with overlapping solar and calibration feeds, flanked by an additional calibration feed, as seen in the left panel of Figure 5. On 2007 November 2, we took three sets of 300 successive 10-s exposures with solar and calibration spectra in separate fibers (hereafter the 2007 data set), as can be seen in the right panels of Figures 3 and 5. In acquiring both data sets, the first five frames of each sequence were discarded to minimize the effect of

persistence due to the usually saturated image that occurs when the detector is not read out for some time.

We made four significant alterations to the instrument setup between these two observations. We (1) altered the fiber setup (as mentioned) to improve S/N in the Th-Ar lines, (2) improved the thermal insulation around the spectrograph to minimize temperature-dependent instrumental drifts, (3) adjusted the wavelength region to minimize the number of telluric features, and (4) swapped a 1300- $\mu\text{m}$  filter for an 1800- $\mu\text{m}$  filter. The last of these modifications enabled us to test suppression of modal noise in the H band by vibration, but significantly increased the thermal background.

While absolute wavelength calibration against a template Th-Ar or iodine absorption is essential for any long-term program, we were interested in looking at changes within a clear observing run. No attempt was made to correct the small departures from linearity present in the raw spectra and establish an absolute wavelength scale in the 2006 data set. Using the calibration lines present and the solar lines, we obtain a scale of  $\sim 2.4 \text{ m s}^{-1}$  per pixel. Figure 6 shows the amplitude of drift in reference lamp lines to be  $\sim 300 \text{ m s}^{-1}$  or 0.12 pixels. The corresponding drift in the solar lines is also shown and can be seen to be of greater magnitude. By subtracting simultaneous pairs of solar-reference points, we account for drifts in the spectrograph, leaving only the radial velocity variation of the Sun due to the Earth's rotation. We ignore the acceleration due to the Earth's elliptical orbit, as well as that due to the apparent motion of the Sun at our latitude due to the obliquity of the ecliptic, as both are small during the observation period.

With the 2007 data set, the same echelle orders were used, but shifted to slightly bluer wavelengths, to increase the number of observed Th-Ar reference lines. The Th-Ar lamp current was also increased to augment the weaker lines. Nevertheless, the few lines and incomplete identification of Th and Ar emission lines in this region of the electromagnetic spectrum only enabled a wavelength calibration using several lines to be made. From Th-Ar and telluric wavelength calibrations, we estimate a pixel resolution of  $2.5 \text{ m s}^{-1}$  for the 2007 instrumental configuration.

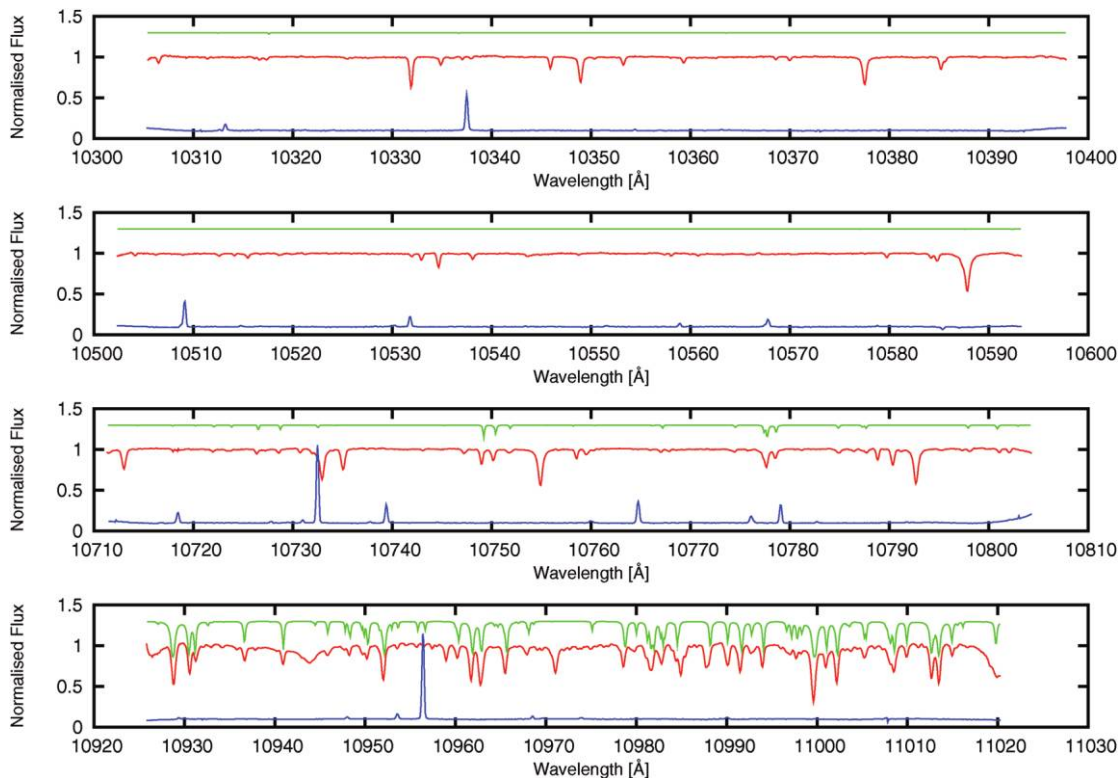


FIG. 4.—Spectra and wavelength coverage of orders 50 (*bottom*) through 53 (*top*) of the 2007 November 2 data set. Within each wavelength region we show the telluric model spectrum (*top curve*), observed (solar and telluric) spectrum (*middle curve*) and the Th-Ar emission reference spectrum divided by a factor of 10 (*bottom curve*).

Both data sets were reduced independently, once with Starlink<sup>4</sup> routines, and again with IRAF<sup>5</sup> routines, for the purpose of comparing the quality of the reduction routines and to help eliminate any systematics that might be introduced in the reduction process. All data were also analyzed using two different cross-correlation routines—HCROSS (using the algorithm developed by Heavens 1993) in Starlink, and FXCOR (Fitzpatrick 1993) in IRAF. The similarity of the results gave us confidence that both packages are viable at this level and our results are sound. In each program, we analyzed regions that were free of obvious telluric contamination, and cross-correlated the individual spectra relative to the first exposure. In the 2006 data set, orders 51 and 52 were used, while in the 2007 data set, orders 50–53 were used. The 2006 and 2007 data sets had 13 and 31 solar lines with absorption features greater than 5% of the continuum, respectively, and 2 and 16 emission lines with more than 1500 counts above background, respectively.

### 3.1. Results and Discussion

Our results are presented in Figure 7, where we have plotted the theoretical and observed radial velocity (RV) curves in the

top panel (providing a  $100 \text{ m s}^{-1}$  offset to the 2006 data set for clarity), and the residuals of the 2006 and 2007 data sets in the middle and bottom panels, respectively. Gaps in the 2006 data set are due to periods of cloud cover, while gaps in the 2007 data set were times during which we took various calibration (flat-field, dark, and wavelength) data. We achieved an overall rms of  $13.1 \text{ m s}^{-1}$  for the 2006 data set. We ignored those intervals where the average pixel counts dropped more than 50% below the mean (i.e., periods of cloud coverage). For the 2007 data set we attain an rms of  $7.1 \text{ m s}^{-1}$  for the second run using FXCOR ( $9.5 \text{ m s}^{-1}$  using HCROSS). Binning the 2007 data in sets of five images improves our results, reducing the rms to  $4.1 \text{ m s}^{-1}$  for the second run, as can be seen in Figure 8. However, binning in sets of  $N$  images does not improve our results as  $\sqrt{N}$ , as would be expected if random error dominated. As we note below, there is a systematic error present that puts a floor on the precision gain from binning. For comparison,  $\sqrt{N}$  plots can be seen in Figure 8. These 1-minute rms values are an order of magnitude above those obtained in the long-running BISON ( $0.2 \text{ m s}^{-1}$ ) and GOLF ( $0.6 \text{ m s}^{-1}$ ) projects (based on Table 1 of Butler et al. 2004). The additional noise in the first run of the 2007 November data is due to the presence of a few scattered clouds, which caused the average pixel counts to vary up to 50%. The second and third run had less than a 1% variation. The third run (with an rms of  $8.5 \text{ m s}^{-1}$ ) shows a distinct

<sup>4</sup> Starlink software is available online at <http://starlink.jach.hawaii.edu/>.

<sup>5</sup> IRAF software is available online at <http://iraf.noao.edu/>.

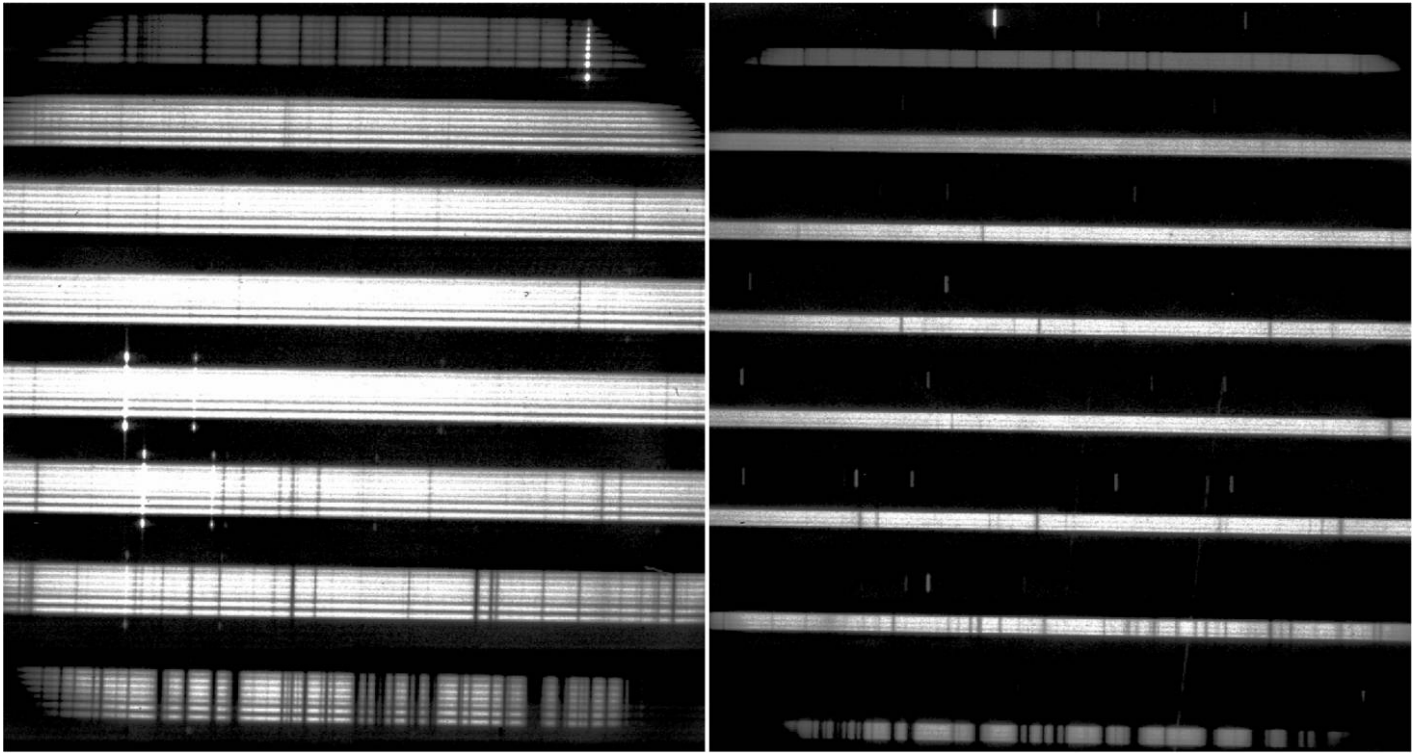


FIG. 5.—Y-band spectrum showing orders 49 (*bottom*) to 56 (*top*) recorded by Pathfinder (*left*: 2006 August; *right*: 2007 November). Wavelengths increase from right to left and from top to bottom. The orders used for the analysis presented are orders 51 and 52 (2006 August) and orders 50–53 (2007 November).

linear trend which also appears (to a lesser extent) in run two. The cause of this trend is not yet understood but clearly something that is monotonic with time and not compensated by the calibration scheme. We are upgrading our system to include

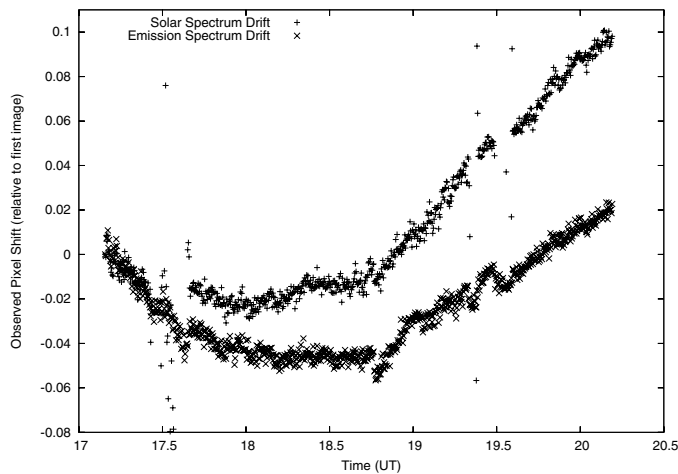


FIG. 6.—Instrumental and solar drift from cross-correlation of order 51 of the 2006 August solar and emission line spectra relative to the first observation. In this figure, a drift of 0.1 pixels corresponds to a change in velocity of  $241 \text{ m s}^{-1}$ . The dominant shape of both curves is due to instrumental drift while the difference in magnitude of the solar drift when compared with the instrumental drift is the result of the Earth’s rotation. Note the breaks in the solar drift caused by the presence of clouds.

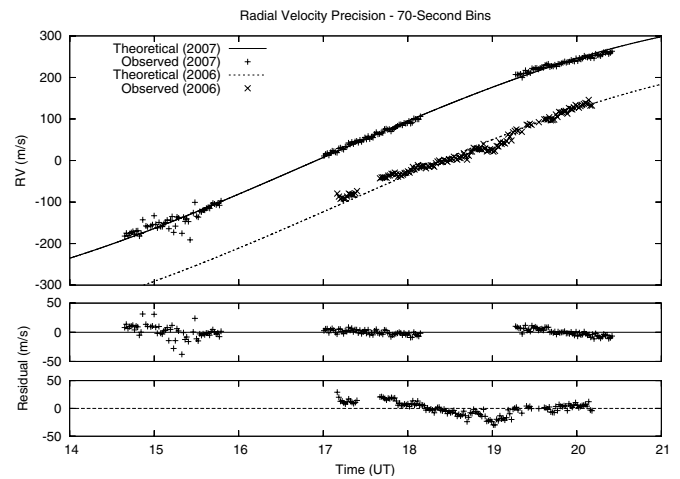


FIG. 7.—Radial velocity of the Sun due to the Earth’s rotation (*top panel*) on 2007 November 2 (*top curve*) and 2006 August 16 (*bottom curve*), binned in groups of five images. The points are the cross-correlation measurements corrected for instrumental drift, which amounted to  $\sim 200 \text{ m s}^{-1}$  (0.083 pixels) over the 3 hr of observations for the 2006 data set and  $\sim 350 \text{ m s}^{-1}$  (0.140 pixels) over 6 hr for the 2007 data set. The measurements have been arbitrarily shifted by small amounts (because we have not performed absolute radial velocity measurements) to best match the theoretical curve. The curves show the predicted sinusoidal variation with respect to apparent solar time. The bottom panels show the residuals for the two data sets.



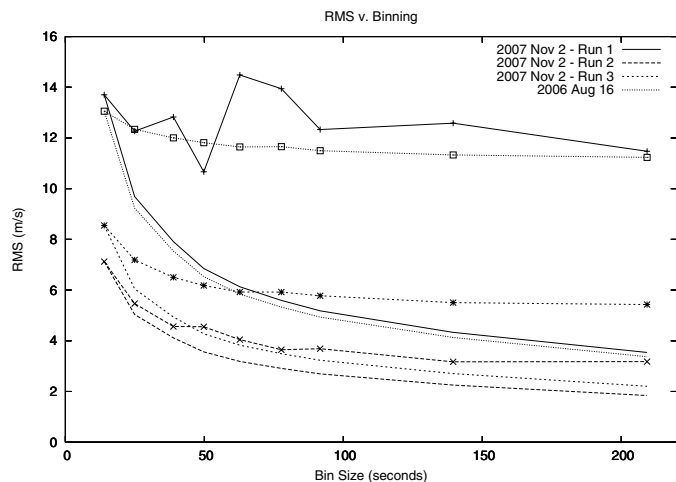


FIG. 8.—rms values in  $\text{m s}^{-1}$  for the three observational sequences of the 2006 and 2007 data sets (with data points) with various amounts of binning, along with the theoretical  $\sqrt{N}$  (no data points) drop in the measured rms for each run. While the exposures are all 10-s each, readout time increases the time between successive images to 14 s.

precision temperature monitoring at several points and, as discussed below, we are also updating our calibration system to aid in minimizing this type of error.

There are a number of reasons to believe that considerable improvements are possible. Our 2007 analysis is based on relatively modest S/N data (for the Sun) and a small wavelength interval. In addition, the Sun has few and relatively weak infrared features. Identical measurements on an M dwarf would yield many more absorption lines, giving rise to a much stronger cross-correlation signature. The use of a larger infrared array and an optimized cross-disperser would allow simultaneous coverage of the Y and J bands, increasing the spectral coverage by approximately a factor of 10 resulting in increased precision.

The greatest improvement will come from using hollow cathode lamps with a larger infrared line density. To this end, we explored the uranium spectra, which revealed 97 Th-Ar lines and 226 U lines between 839.5 to 897.5 nm (Palmer et al. 1980). This encouraged us to procure a U-Ar hollow cathode lamp; a preliminary observation in the Y band revealed a similar 2:1 ratio of U to Th lines. Using both lamps simultaneously in future experiments will undoubtedly improve our measured precision.

#### 4. CONCLUSION

For the first time in the NIR, we have demonstrated rms radial velocity precisions below  $10 \text{ m s}^{-1}$  over a period of several hours, using 10-s observations of the Sun. There are a number of improvements that we hope to implement when additional funding is secured. Foremost is to install a R4 echelle appropriately sized and a volume phase holographic (VPH) or standard cross-disperser grating optimized for the 1–1.3  $\mu\text{m}$  region. These two items in themselves will lead to close to an order of magnitude increase in throughput. In addition, we will update our calibration system to allow us to move from precision acceleration measurements over a short period of time to precise velocity measurement over weeks to months. The upgraded calibration system will include both Th-Ar and U-Ar hollow cathode lamps as well as a gas cell that is illuminated by a Q-I lamp. While we do not intend to use a gas cell simultaneously in line with the object observations as pioneered by Butler et al (1996) in the visible, it will allow a better absolute velocity determinations as well as a means to track systematics in the hollow cathode lamps. We are implementing the capability to rapidly switch between the target spectrum and the gas cell to allow calibrations between target spectra. We will initially test HF and water vapor gas cells in the 1.0 to 1.25  $\mu\text{m}$  range but note that no single gas has a large number of deep lines over the desired wavelength range. Adding the U-Ar hollow cathode lamp will increase the number of lines at least a factor of 2 and allow less dependence on Ar lines. We also will investigate the effects persistence may have on the achievable precision. With the noted improvements we will be ready to move this instrument to the Hobby-Eberly Telescope for tests on M dwarfs to firmly establish the viability of NIR precision radial velocity spectroscopy in these objects.

The effort through September 2006 was partially supported by a Gemini Design Study for the Precision Radial Velocity Spectrometer and National Science Foundation Grant AST06-07634. We acknowledge many valuable conversations with other members of the PRVS team, in particular, John Rayner, Bill Dent, Adrian Webster and Chris Tinney. We also acknowledge the continuing encouragement by Gemini. H. R. A. Jones and J. Barnes are supported by PPARC grant PP/D0000920/1. Finally, we thank Don Schneider and NSF Grant AST03-07582 for their support.

#### REFERENCES

- Baudrand, J., Walker, G. A. H. 2001, *PASP*, 113, 851  
 Becker, J. M. 1976, *Nature*, 260, 227  
 Blake, C. H., Charbonneau, D., White, R. J., Marley, M. S., & Saumon, D. 2007, *ApJ*, 666, 1198  
 Butler, R. P., Marcy, G. W., Williams, E., McCarthy, C., Dosanji, P., & Vogt, S. S. 1996, *PASP*, 108, 500  
 Butler, R. P., et al. 2004, *ApJ*, 600, L75  
 Campbell, B., & Walker, G. A. H. 1979, *PASP*, 91, 540  
 Campbell, B., Walker, G. A. H., & Yang, S. 1988, *ApJ*, 331, 902  
 Deckker, H. et al. 2000, *Proc. SPIE*, 4008, 534  
 Fitzpatrick, M. J. 1993, in *ASP Conf. 52, Astronomical Data Analysis Software and Systems II*, ed. R. J. Hanisch, R. J. V. Brissenden, & J. Barnes (San Francisco: ASP), 472  
 Gray, D. F., & Brown, K. I. T. 2006, *PASP*, 118, 399  
 Heavens, A. F. 1993, *MNRAS*, 263, 735  
 Hinkle, K. H. et al. 2003, *Proc. SPIE*, 4834, 353

- Johnston, K. 2006, MSci Project, University of St. Andrews
- Kasting, J. F., & Catling, D. 2003, *ARA&A*, 41, 429
- Koch, A., & Woehl, H. 1984, *A&A*, 134, 134
- Martin, E., et al. 2006, *ApJ*, 644, L75
- McLean, I. et al. 1998, *Proc. SPIE*, 3354, 566
- Palmer, B. A., Keller, R. A., & Engleman, R. 1980 Los Alamos Informal Report LA-8251-MS
- Pepe, F. et al. 2000, *Proc. SPIE*, 4008, 582
- Schroeder, D.J. 2000, *Astronomical Optics* (San Diego: Academic Press)
- Stassun, K. J., Mathieu, R. D., & Valenti, J. A. 2006, *Nature*, 440, 311
- Tinney, C.G. et al. 2001, *ApJ*, 551, 507
- Tull, R. G. 1998, *Proc. SPIE*, 3355, 387
- Vogt, S. S. et al. 1994, *Proc. SPIE*, 2198, 362
- Wolszczan, A., & Frail, D. A. 1992, *Nature*, 355, 145